

A hybrid prediction method for low-subsonic turbulent flow noise

Y.J. Moon^{a,*}, J.H. Seo^a, Y.M. Bae^a, M. Roger^b, S. Becker^c

^a Department of Mechanical Engineering, Korea University, Seoul 136-701, Republic of Korea

^b Laboratoire de Mécanique des Fluides et Acoustique (LMFA), Ecole Centrale de Lyon, 69134 Ecully, France

^c Institute of Fluid Mechanics, University Erlangen-Nuremberg, 91058 Erlangen, Germany

ARTICLE INFO

Article history:

Received 7 October 2008

Received in revised form 26 January 2010

Accepted 17 February 2010

Available online 6 March 2010

Keywords:

Turbulent noise

Low subsonic flow

LES/LPCE hybrid method

ABSTRACT

A hybrid method is proposed for prediction of low-subsonic, turbulent flow noise. In this method, the noise sources in the near wall turbulences or in the wake are computed by the incompressible large eddy simulation (LES), while the generation and propagation of the acoustic waves are solved by the linearized perturbed compressible equations (LPCE), with acoustic sources represented by a material derivative of the hydrodynamic pressure, DP/Dt . The accuracy of the present method is critically assessed for two experiments conducted at the Ecole Centrale de Lyon and the University Erlangen, where aeroacoustic measurements were taken for (i) the flat plate self-noise at zero angle of attack ($Re_c = 1.3 \times 10^5$, $M = 0.06$) and (ii) the forward-facing step noise ($Re_h = 8000$, $M = 0.03$), respectively. The noise sources are identified and analyzed further to determine their spectral-dependent, spanwise coherence functions, γ_{ij} of the wall pressure fluctuations, in order to quantify the sizes of the noise sources. The far-field sound pressure level (SPL) spectra predicted by the present method are found in excellent agreement with the experimental measurements.

© 2010 Elsevier Ltd. All rights reserved.

1. Introduction

Prediction of turbulent flow noise is one of the main challenges in computational aeroacoustics; for example, jet noise, airframe noise, etc. Difficulties are associated with not only identifying the noise sources but also resolving their spatio-temporal scales because they are strongly dependent on the Reynolds number and the Mach number.

Our present interests are focused on prediction of low-subsonic, turbulent flow noise, such as airframe noise at landing, automobile wind noise, and fan noise. In these cases, Reynolds numbers are usually in the order of millions but Mach numbers are less than 0.1 or 0.2 at the largest. The noise sources are highly localized in the turbulent boundary layer near the wall or in the wake, while the acoustic wavelengths far exceed the hydrodynamic length scales. For such multi-scale problem, direct numerical simulation (DNS) employing the full compressible Navier–Stokes equations becomes very difficult and expensive, coping with the fact that a long-time computation is often required to represent the turbulence statistics, i.e. noise sources.

A hybrid approach has been sought as an alternative. This method is based on a hydrodynamic/acoustic splitting method proposed by Hardin and Pope [1]. The hydrodynamic flow field is solved by the incompressible Navier–Stokes equations, while the acoustic field is computed by the perturbed Euler equations with acoustic

sources. It is, however, found that the original formulation as well as other modified forms [2,3] yield inconsistent acoustic solutions when a noise source is in the shear flow. This is due to the unstable vortical mode that can be excited by the non-linear terms in the perturbed momentum equations. These terms are actually the source terms in the perturbed vorticity transport equations. In the previous studies [4,5], it has been shown that the vortical instability occurs when the source terms are improperly treated by either lack of physical diffusion or lack of grid resolution of the perturbed vorticity ($\vec{\omega}' = \nabla \times \vec{u}'$). Here, the prime denotes an instantaneously perturbed quantity from an incompressible state. A similar observation was also made by Ewert and Schröder [6] for developing a hybrid method of various forms with careful consideration of stability issues. To avoid such a problem, the linearized perturbed compressible equations (LPCE) [5] have been formulated by eliminating the terms related to the generation of the perturbed vorticity. The stability and accuracy of the LPCE method has been validated for some benchmark problems, comparing with DNS and analytical solutions. Besides, it has been shown that the upper Mach number limit for the LPCE method can be high as 0.5 for a laminar dipole tone from a 2D cylinder cross-flow [5].

In the present study, we propose a hybrid method for prediction of low-subsonic, turbulent flow noise. Here, the noise sources in the near wall turbulences or in the wakes are computed by the incompressible large eddy simulation (LES), while the generation and propagation of the acoustic waves are solved by the LPCE, with acoustic sources (DP/Dt) acquired from the incompressible LES solutions. The proposed LES/LPCE hybrid method is computation-

* Corresponding author.

E-mail address: yjmoon@korea.ac.kr (Y.J. Moon).

ally efficient, especially at low Mach numbers because it is based on an incompressible flow solver and the grid systems for flow and acoustics can be treated differently. As an example, an acoustic grid at the wall can be much larger than that of the hydrodynamic grid, which typically requires $\Delta y^+ < 1-2$ to resolve the turbulent boundary layer. With this grid-splitting technique, the time step restricted by a CFL condition can be largely relieved and thereby the afore-mentioned scale-disparity problem can be substantially reduced [4].

The present LES/LPCE hybrid method is validated for two low-subsonic, turbulent flow noise experiments conducted respectively at the Ecole Centrale de Lyon and the University Erlangen: (i) flat plate self-noise at zero angle of attack ($Re_c = 1.3 \times 10^5$, $M = 0.06$) [7] and (ii) forward-facing step noise ($Re_h = 8000$, $M = 0.03$) [8]. The flat plate has ‘well-known’ noise sources at the trailing-edge: a tonal peak by the vortex shedding and the broadband noise via edge-scattering of the convecting eddies in the turbulent boundary layer. In this case, the tone is spectrally broadened by the spanwise instability of the separated shear-layer [9,10] and the spectral determination of the spanwise coherence length is considered one of the most important parts, as far as prediction of the far-field sound pressure level (SPL) spectrum is concerned. In the latter experiment, noise generation is generally associated with unsteadiness of the leading-edge separation bubble over the step, but the noise generation mechanisms are not fully understood in details. The key issue is how to link the forward-facing step noise with the involved unsteady flow characteristics such as the shear-layer flapping, the shear layer instability, the eddy-wall interactions at the reattachment point, and the bifurcating nature of the re-circulating zone in front of the step [11].

In Section 2, computational methods for flow and acoustics are introduced, and two afore-mentioned experimental works are briefly described in Section 3. In Section 4, the accuracy of the present LES/LPCE hybrid method is assessed and noise sources and noise generation mechanisms are discussed.

2. Computational methodologies

2.1. LES/LPCE hybrid method

The present LES/LPCE hybrid method is based on a hydrodynamic/acoustic splitting method [1], in which the total flow variables are decomposed into the incompressible and perturbed compressible variables as,

$$\begin{aligned} \rho(\vec{x}, t) &= \rho_0 + \rho'(\vec{x}, t) \\ \vec{u}(\vec{x}, t) &= \vec{U}(\vec{x}, t) + \vec{u}'(\vec{x}, t) \\ p(\vec{x}, t) &= P(\vec{x}, t) + p'(\vec{x}, t). \end{aligned} \quad (1)$$

The incompressible variables represent hydrodynamic flow field, while acoustic fluctuations and other compressibility effects are resolved by perturbed quantities denoted by ($'$).

The hydrodynamic turbulent flow field is first solved by incompressible LES. The filtered incompressible Navier–Stokes equations are written as,

$$\frac{\partial \tilde{U}_j}{\partial x_j} = 0 \quad (2)$$

$$\rho_0 \frac{\partial \tilde{U}_i}{\partial t} + \rho_0 \frac{\partial}{\partial x_j} (\tilde{U}_i \tilde{U}_j) = -\frac{\partial \tilde{P}}{\partial x_i} + \mu_0 \frac{\partial}{\partial x_j} \left(\frac{\partial \tilde{U}_i}{\partial x_j} + \frac{\partial \tilde{U}_j}{\partial x_i} \right) - \rho_0 \frac{\partial}{\partial x_j} M_{ij}, \quad (3)$$

where the grid-resolved quantities are denoted by (\sim) and the unknown sub-grid tensor M_{ij} is modeled as

$$M_{ij} = \tilde{U}_i \tilde{U}_j - \tilde{U}_i \tilde{U}_j = -(C_s \Delta)^2 |\tilde{S}| \tilde{S}_{ij}. \quad (4)$$

Here, Δ is a mean radius of the grid cell (computed as cubic root of its volume), \tilde{S}_{ij} is the strain-rate tensor.

After a quasi-periodic stage of hydrodynamic field is attained, the perturbed quantities are computed by the linearized perturbed compressible equations (LPCE). A set of the linearized perturbed compressible equations is written in a vector form as,

$$\frac{\partial p'}{\partial t} + (\vec{U} \cdot \nabla) p' + \rho_0 (\nabla \cdot \vec{u}') = 0 \quad (5)$$

$$\frac{\partial \vec{u}'}{\partial t} + \nabla (\vec{u}' \cdot \vec{U}) + \frac{1}{\rho_0} \nabla p' = 0 \quad (6)$$

$$\frac{\partial p'}{\partial t} + (\vec{U} \cdot \nabla) p' + \gamma P (\nabla \cdot \vec{u}') + (\vec{u}' \cdot \nabla) P = -\frac{DP}{Dt}. \quad (7)$$

The left-hand side of LPCE represents effects of acoustic wave propagation and refraction in an unsteady, inhomogeneous flow, while the right-hand side only contains an acoustic source term, which is projected from the incompressible LES flow solution. It is interesting to note that for low Mach number flows, the total change of the hydrodynamic pressure, DP/Dt is only considered as the explicit noise source term.

Because a curl of the linearized perturbed momentum equations, Eq. (6) yields

$$\frac{\partial \vec{\omega}'}{\partial t} = 0, \quad (8)$$

the LPCE prevents any further changes (generation, convection, and decaying) of perturbed vorticity in time. In fact, the perturbed vorticity could generate self-excited errors, if $\vec{\omega}'$ is not properly resolved with the acoustic grid. Hence, the evolution of the perturbed vorticity is pre-suppressed in LPCE, deliberating the fact that the perturbed vorticity has little effects on noise generation, particularly at low Mach numbers. For hybrid methods [5,6], this is an important property that ensures consistent, grid-independent acoustic solutions. Derivation of LPCE and the detailed discussion on characteristics of the perturbed vorticity can be found in Ref. [5].

The filtered incompressible Navier–Stokes equations are solved by an iterative fractional-step method (Poisson equation for the pressure), whereas the linearized perturbed compressible equations are solved in a time-marching fashion. To avoid excessive numerical dissipations and dispersions errors, the governing equations are spatially discretized with a sixth-order compact finite difference scheme [12] and integrated in time by a four-stage Runge–Kutta method. For example, the first and second derivatives with respect to x are implicitly calculated with a five-point stencil, i.e.

$$\alpha_1 f'_{i-1} + f'_i + \alpha_1 f'_{i+1} = a_1 \frac{f_{i+1} - f_{i-1}}{2\Delta x} + b_1 \frac{f_{i+2} - f_{i-2}}{4\Delta x} \quad (9)$$

$$\alpha_2 f''_{i-1} + f''_i + \alpha_2 f''_{i+1} = a_2 \frac{f_{i+1} - 2f_i + f_{i-1}}{\Delta x^2} + b_2 \frac{f_{i+2} - 2f_i + f_{i-2}}{4\Delta x^2}, \quad (10)$$

where $\alpha_1 = 1/3$, $\alpha_2 = 2/11$, $a_1 = 14/9$, $b_1 = 1/9$, $a_2 = 12/11$, and $b_2 = 3/11$. Practically, when using a high order scheme to the stretched meshes, numerical instability are encountered due to numerical truncations or failure of capturing high wave-number phenomena. Thus, a tenth-order spatial filtering (cut-off wave number, $k\Delta x \approx 2.9$) proposed by Gaitonde et al. [13] is applied every iteration to suppress the high frequency errors that might be caused by grid non-uniformity. For the far-field boundary condition, an energy transfer and annihilation (ETA) boundary condition [14] with buffer zone is used for eliminating any reflection of the out-going waves. The ETA boundary condition is easily facilitated with a rapid grid stretching in a buffer-zone and the spatial filtering which is damping out waves shorter than grid spacing. So, if a buffer-zone has grid spacing larger than out-going acoustic wave length, the wave can be successfully absorbed by the ETA boundary condition.

2.2. Computation of far-field acoustics

The two experiments conducted at the Ecole Centrale de Lyon and the University Erlangen are concerned with low-subsonic, turbulent flows, which are statistically homogeneous in the spanwise direction over a long span. Hence, incompressible LES is conducted for a short simulated span (L_s), in which the spanwise-correlated flow structures are computed by imposing a periodic boundary condition at the side boundaries. In LPCE calculation, however, the periodic boundary condition cannot be applied for the same simulated span because it results in un-physically correlated acoustic forcing [15–17]. One could use an absorbing boundary condition at the spanwise boundaries [18] but flow and acoustics both require three-dimensional computations.

Here, a computationally more efficient approach is pursued (see Fig. 1). A two-dimensional acoustic field (at the zero spanwise wave number, $k_z = 0$) is calculated at the mid-span plane with acoustic sources and hydrodynamic variables integrated in the spanwise direction; $\bar{q}(x, y, t) = \int_0^{L_s} q(x, y, z, t) dz$, where L_s is the span used for LES. The computed far-field acoustic pressure is then corrected by the following relation. Considering an acoustic wave equation which is Fourier-transformed in the spanwise direction, a three-dimensionally radiated far-field acoustic pressure in frequency domain, \hat{p}' is related to a two-dimensionally predicted acoustic pressure at $k_z = 0$, \hat{p}' by

$$\hat{p}'(x, y, 0, \omega) \approx \bar{\hat{p}}'(x, y, \omega) \frac{1+i}{2} \sqrt{\frac{\omega}{c_0 \pi r}} \quad (11)$$

where c_0 is a speed of sound at ambient condition. Derivation of this relation proposed by Oberai et al. may be found in reference [19]. Here, it is important to note that the strength of the noise source is directly incorporated with the spanwise coherence length-scale of the flow, when variables are spanwise-averaged at the mid-span plane.

At low Mach numbers, acoustic waves generated in the stream of turbulences have a range of wavelengths, all of which are difficult to resolve unless grids are really fine up to the far-field boundary. If an observer's position is far from the noise source, an acoustic domain can be truncated and the acoustic pressure obtained by LPCE can be extrapolated from the truncated boundary to the far-field observer's position by a 2D Kirchhoff method [20],

$$4i\hat{p}' = - \int_S \left[\frac{\partial \hat{p}'}{\partial n} H_0^{(2)}(\omega r/c_0) - \frac{\omega}{c_0} (\hat{n} \cdot \hat{r}) \hat{p}' H_1^{(2)}(\omega r/c_0) \right] dS, \quad (12)$$

where r is the distance from the source to the observer's position, \hat{n} is a unit vector normal to the Kirchhoff surface, and $H_j^{(2)}$ is the Hankel function of order j and second kind. In Eq. (12), the effect of the

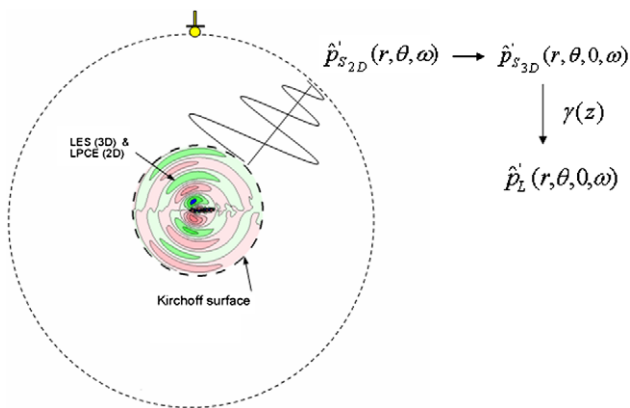


Fig. 1. Schematic of computing far-field acoustics for the long-span body.

momentum fluctuations (Lighthill stress tensor) is neglected because the Kirchhoff surface is usually set in the mid-field, where the momentum fluctuations are negligible.

So far, it is described how to compute the sound pressure level (SPL) at the far-field with the simulated span (L_s). In order to estimate the SPL for the entire span (L) used in the experiment, the SPL for the simulated span must be corrected. In this section, a correction method is employed, which is re-formulated by Seo and Moon [21], revisiting the previous works of Kato et al. [22] and Perot et al. [15]. Here, a long-span body is divided into N subsections by L_s (i.e. $L = N \cdot L_s$) and let the spectral acoustic pressure radiated from the i -th subsection be \hat{p}'_i . Then, the power spectral density of acoustic pressure for the entire span, \hat{p}'_L can be written as

$$\hat{p}'_L \hat{p}'_L^* = \sum_{i=1}^N \hat{p}'_i \cdot \sum_{j=1}^N \hat{p}'_j^* = \sum_{i=1}^N \sum_{j=1}^N \text{Re}(\hat{p}'_i \hat{p}'_j^*), \quad (13)$$

where $*$ denotes a complex conjugate. Now, let the assumption of 'statistical homogeneity in the spanwise direction' satisfy the following properties for the simulated span, L_s ; (i) the power spectral density of the acoustic pressure radiated from each subsection is the same, (ii) the acoustic pressure radiated from each subsection is only lagged by a phase difference, (iii) the phase lagging is a function of the spanwise separation between two subsections, Δz_{ij} .

In many cases, these assumptions are not so crude, if the observer's position is sufficiently far. By employing the afore-mentioned properties, the power spectral density of the acoustic pressure emitted from the entire span, Eq. (13) can be written as

$$|\hat{p}'_L|^2 = \sum_{i=1}^N \sum_{j=1}^N \gamma'(\Delta z_{ij}) \cdot |\hat{p}'_s|^2, \quad (14)$$

where \hat{p}'_s is the spectral acoustic pressure radiated from L_s and $\gamma'(\Delta z_{ij})$ is the acoustic spanwise coherence function. So, one can now estimate $|\hat{p}'_L|^2$ by determining $\gamma'(\Delta z_{ij})$. Since the phase lagging in the spanwise direction tends to follow a Gaussian distribution [9,10], the acoustic spanwise coherence function, $\gamma'(\Delta z_{ij})$ can be expressed as

$$\gamma'(\Delta z_{ij}) = \exp\left(-\frac{\Delta z_{ij}^2}{L'_c(\omega)^2}\right), \quad (15)$$

where $L'_c(\omega)$ is the spanwise coherence length.

From Eqs. (14) and (15), the SPL to be corrected for the long-span body is given by

$$\text{SPL}_c(\omega) = 10 \log \left[\sum_{i=1}^N \sum_{j=1}^N \exp\left(-\frac{(i-j)^2 \left(\frac{L_s}{L'_c(\omega)}\right)^2}{2}\right) \right]. \quad (16)$$

Eq. (16) can be approximated to a simpler form (dashed lines in Fig. 2), which might be useful for engineering purposes:

$$\text{SPL}_c = \begin{cases} 10 \log N & (L'_c/L_s \leq 1/\sqrt{\pi}) \\ 10 \log(L'_c/L_s) + 10 \log(\sqrt{\pi} N) & (1/\sqrt{\pi} < L'_c/L_s < N/\sqrt{\pi}) \\ 20 \log N & (L'_c/L_s \geq N/\sqrt{\pi}). \end{cases} \quad (17)$$

It is interesting to note that Eq. (16) or (17) has the same asymptotic behavior as Kato's formula and also that Eq. (17) can be still useful for small N , as long as L'_c/L_s is not too large, for example, less than 3.

As shown above, determining $L'_c(\omega)$ from the acoustic spanwise coherence function, $\gamma'(\Delta z_{ij})$ is an important step for estimating $\text{SPL}_c(\omega)$. Actually, $\gamma'(\Delta z_{ij})$ is difficult to measure experimentally because the acoustic far-field cannot be windowed (or sectioned) by L_s for the entire span. Alternatively, it can be estimated by an acoustic analogy with the computed (or measured) surface

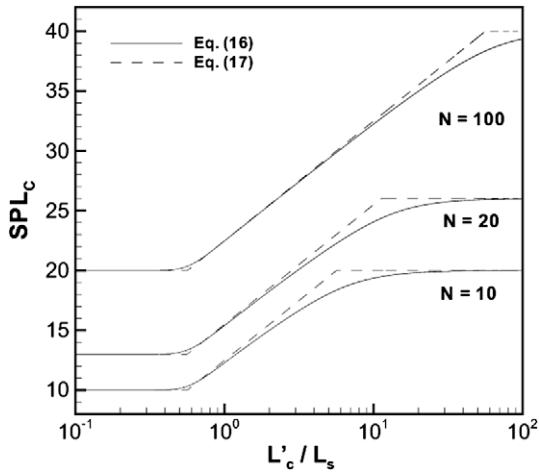


Fig. 2. SPL correction for the long-span body.

pressure data [15]. The cross-power spectrum $\hat{p}'_i \hat{p}'_j$ can be evaluated with the surface pressure, using the Curle's analogy solution:

$$\hat{p}'(\omega) \simeq \frac{1}{4\pi c_0} \int (\vec{r} \cdot \hat{n}) (-i\omega \hat{P}(\omega)) \exp(i\omega r/c_0) dS. \quad (18)$$

For a compact source or when the observer's position is very far, it can be assumed that $r/c_0 \approx \text{constant}$. Then, the cross-power spectrum $\hat{p}'_i \hat{p}'_j$ is analytically written as

$$\hat{p}'_i \hat{p}'_j \simeq \left| \frac{-i\omega \exp(i\omega r/c_0)}{4\pi c_0} \right|^2 \int (\vec{r} \cdot \hat{n}) \hat{P}_i dS_i \cdot \int (\vec{r} \cdot \hat{n}) \hat{P}_j dS_j \quad (19)$$

and the acoustic spanwise coherence function can be expressed as

$$\gamma'(\Delta z_{ij}) \simeq \frac{\text{Re} \left(\int (\vec{r} \cdot \hat{n}) \hat{P}_i dS_i \cdot \int (\vec{r} \cdot \hat{n}) \hat{P}_j dS_j \right)}{\sqrt{\left| \int (\vec{r} \cdot \hat{n}) \hat{P}_i dS_i \right|^2} \sqrt{\left| \int (\vec{r} \cdot \hat{n}) \hat{P}_j dS_j \right|^2}}, \quad (20)$$

where \hat{P}_i is the surface pressure at each subsection and $\int dS_i$ is the surface integral over each subsectional area. Eq. (20) is the relation between the acoustic spanwise coherence function, $\gamma'(\Delta z_{ij})$ and the spanwise coherence function of the 'integrated' surface pressure. For a certain application, it is also possible to replace $\gamma'(\Delta z_{ij})$ by the spanwise coherence function of the surface pressure at a point of interest, and such a coherence function can be easily computed or measured by experiments. More detailed discussion can be found in Ref. [21].

3. Experiments

3.1. Flat plate self-noise

The experiment has been performed in the low-speed (20–40 m/s), open-jet anechoic wind tunnel of the Ecole Centrale de Lyon (ECL). As shown in Fig. 3, the investigated rectangular model plate is held vertically between horizontal side-plates fixed to the nozzle, and the angle of attack of the plate can vary from 0° to 10° . It has a thickness of 3 mm, a chord length of 10 cm and a spanwise extent of 30 cm. It is rounded at the edge corners by a bevel of radius 0.5 mm in order to smoothen the geometrical singularities. The acoustic measurements are made at a distance 2 m from the trailing edge in the mid-span plane by a single B&K 1/2" microphone on a rotating support [7]. All results correspond to a pressure PSD in decibels per Hz, with a reference pressure of 0.00002 Pa, and the data have been averaged on 200 samples, over

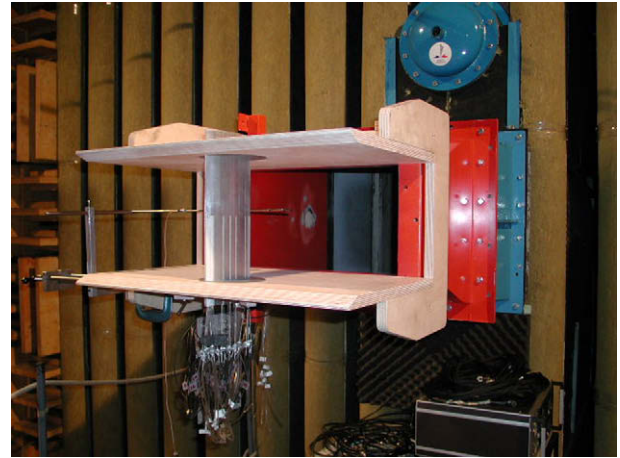


Fig. 3. ECL experimental setup showing the instrumented plate and the side-plates fixed to the nozzle.

the frequency range 0–12,800 Hz, with a frequency-band 4 Hz and Hanning windowing.

3.2. Forward-facing step noise

Measurements are carried out in an aeroacoustic wind tunnel at the University Erlangen, which is integrated into an anechoic chamber. The chamber has a lower cut-off frequency of 300 Hz. The anechoic environment allows for the measurement of the directional pattern of the radiated sound. The closed circuit wind tunnel has an open test section with a nominal cross-section of 200 mm × 260 mm and yields a maximum exit velocity of 50 m/s. For the experiments described, a larger nozzle with a cross section of 250 mm × 0330 mm is used and the velocity ranges from 10 m/s to 30 m/s. The free stream turbulence ratio is found to be 0.15% for the respective velocities [8]. Fig. 4 shows the general measurement setup, where a flat plate (length 1 m in streamwise direction, width 0.66 m) is flush mounted to the nozzle. At 370 mm downstream of the nozzle, a step with a sharp upper edge is attached to the plate. Different measurements have been taken for flows with Reynolds numbers Re_h (based on step height, h) ranging from 8000 to 24,000. The step height, h is 12 mm for all experiments. Using a microphone placed outside the flow, the flow-induced noise field of the forward facing step is recorded at

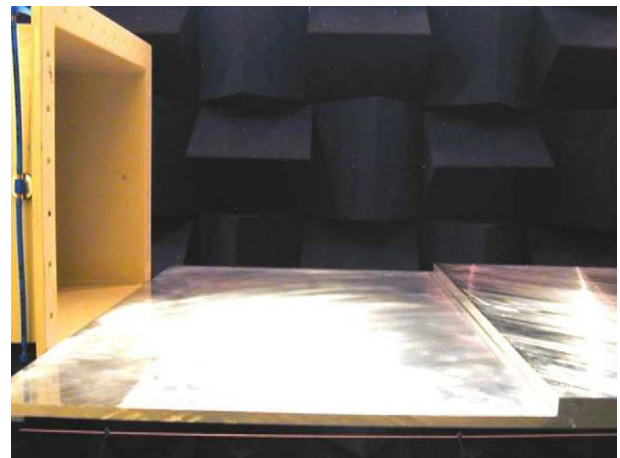


Fig. 4. University Erlangen experimental setup showing a step over the plate, flush-mounted on the nozzle.

a distance of 1 m right above the step-edge. For each velocity, the acoustic measurement is carried out twice. First, the step is removed and the background noise stemming from tunnel and plate is recorded. Then the step is mounted on the plate and the measurement is repeated. The respectively recorded spectra show clearly the noise contributed by the step.

4. Results and discussion

4.1. Flat plate self-noise

This case considers a flow ($U_0 = 20$ m/s) over the flat plate at zero angle of attack (experiment described in Section 3.1). The plate has a chord length of $c = 10$ cm with thickness $h = 0.03c$ and span $L = 3c$. The Reynolds number of the flow based on the chord length, Re_c is 1.3×10^5 and the Mach number, M_0 is 0.06. For incompressible large eddy simulation, an o-type grid is employed to treat four rounded-corners of the leading and trailing edges (see Fig. 5). The computational domain is set to $r = 10c$ and a spanwise extension is chosen as 3% of the plate chord with flow periodicity assumed at the side boundaries. The computational domain is consisted of $657 \times 201 \times 21$ (about 2.8 millions) points in x , y , and z and is divided into 32 blocks for parallel computations. A minimal grid size for x and y is $0.0005c$ (or $\Delta x_{min}^+ = \Delta y_{min}^+ \simeq 3$), while a uniform grid spacing of $0.0015c$ (or $\Delta z^+ \simeq 15$) is used in the spanwise direction. The computation is conducted with $\Delta t = 1 \times 10^{-6}$ s for 400,000 iterations (or 0.4 s), and no sub-grid scale (SGS) model is used. It was shown by Visbal and Rizetta [23], testing with isotropic turbulence, that the tenth-order spatial filtering used in the present study has a cut-off wave number, $k\Delta x \approx 2.9$, which far exceeds the test-filter width of $k\Delta x = \pi/2 \approx 1.57$ and therefore only damps out the scales that are un-resolved by the sixth-order compact differencing scheme.

Fig. 6 shows the flow structures over the plate by the instantaneous spanwise vorticity. The leading-edge separation bubble triggers the boundary layer at $x = 0.2c$ and makes the downstream boundary layer turbulent. The iso-surfaces of the second invariant property of the velocity gradients ($Q = 200$) clearly shows the noise sources, i.e. convecting turbulent eddies within the boundary layer and the vortex shedding at the trailing-edge. It was found that the thickness of the boundary layer, δ is $1.12h$ at $x = -0.2c$ from the trailing-edge and the turbulent Reynolds number, Re_τ is approximately 230.

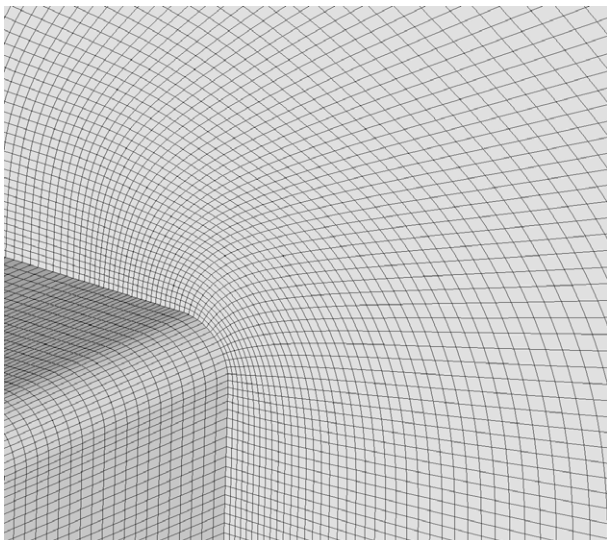


Fig. 5. Grid details near the trailing-edge of the flat plate.

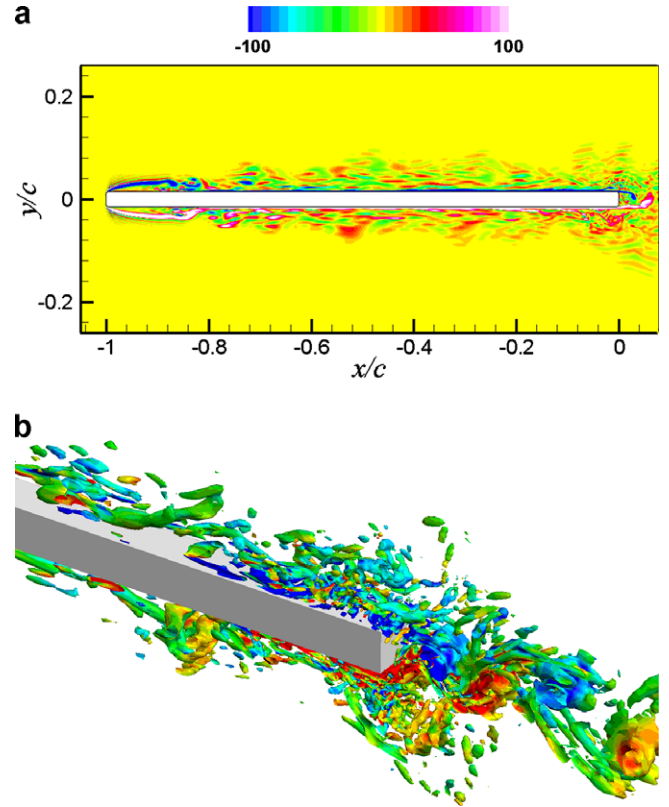


Fig. 6. Instantaneous spanwise vorticity contours at the mid-span (top); instantaneous Q iso-surfaces around the trailing-edge (bottom).

The wall pressure fluctuations over the plate are monitored along the plate. The boundary layer at $-0.2c$ from the trailing-edge is expected to be turbulent. The power spectral density (PSD) spectrum of the wall pressure fluctuations scaled on inner flow variables is compared in Fig. 7 with the DNS data of Na and Moin [24] and the experimental data of Farabee and Casarella [25]. The present LES solution indicates a weak influence of the trailing-edge on the PSD spectrum: a small peak at $St (= fh/U_0) = 0.2$ by the vortex shedding and an effect of very mild pressure gradient. On the other hand, the overall profile closely matches the PSD spectrum

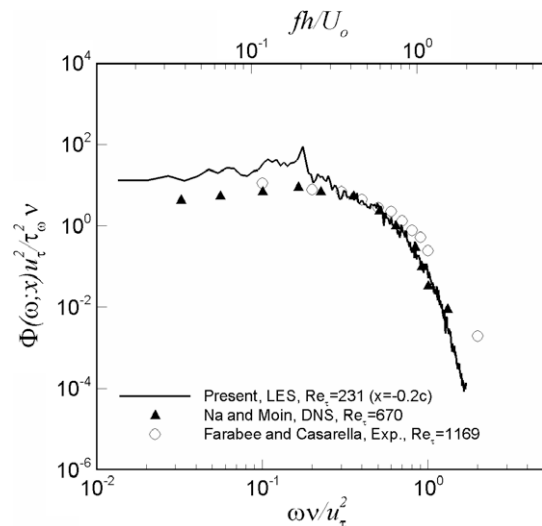


Fig. 7. Power spectral density spectra (inner-scaled) of wall pressure fluctuations at $x/c = -0.2$, compared with DNS and experiment.

of a fully turbulent boundary layer over the flat plate (with zero pressure gradient). One can notice that the temporal scales are only resolved up to Strouhal number close to 2. As a reference, turbulent eddies fluctuating around $St = 1$ are viscously dissipated within the boundary layer because $St = 1$ is close to $\omega\nu/u_\tau^2 \approx 1$, as indicated in Fig. 7.

Fig. 8 shows the wall pressure PSD spectra at three different locations, $x = -0.8c$, $-0.5c$, and $-0.02c$. At $x = -0.02c$, the effect of vortex shedding is clearly pronounced showing a spectrally-broadened peak at $St = 0.2$ and the eddies dissipating around $St = 1$ change the decaying rate from -2.3 to $-5/3$. So one can conjecture that those small-scale eddies also make contributions partially to the high frequency noise, when they get scattered at the trailing-edge. It is also observed that at $x = -0.8c$ (reattachment point), the leading-edge separation bubble generates a PSD level of wall pressure fluctuations even higher than the peak at the vortex shedding frequency. So, it is questioned whether this is a possible noise contributor or not, and it will be discussed later with the far-field SPL spectrum analysis.

The flat plate self-noise is now computed by the linearized perturbed compressible equations (LPCE). The LPCE computation is carried out with the same time step (i.e. $\Delta t = 1 \times 10^{-6}$ s) for the last 200,000 iterations (or 0.2 s) of LES data. An o-type, acoustic grid (347×247) is used with minimal normal spacing at the wall five times larger than that of the hydrodynamic grid. The acoustic grid has the same domain extent as the hydrodynamic grid ($r = 10c$), and those waves propagating farther to the far-field at the microphone location ($r = 20c$) are emulated by the 2D Kirchoff method. To interpolate the source terms and the hydrodynamic variables onto the acoustic grid, we employed a bi-linear shape function in space. This bi-linear interpolation maintains sufficient accuracy when a fine hydrodynamic grid solution is interpolated onto the coarse acoustic grid, and this is always the case for the present hybrid method.

An instantaneous pressure fluctuation field ($\Delta p' = (P + p') - \overline{(P + p')}$) around the plate in Fig. 9 clearly shows the radiation of the dipole tone generated by the vortex shedding at the trailing-edge. The acoustic wavelength of the tone is close to $\lambda/c = 2.5$, corresponding to the frequency $St = 0.2$ at $M_o = 0.06$. Besides, the figure shows other high frequency waves being emanated from the trailing-edge as well as from the shear-layer reattachment point. There will also be the waves diffracted at the leading and trailing-edge of the plate, and all of these will contribute in part to the far-field noise measured at the microphone location (see Fig. 11).

In order to predict the far-field SPL spectrum, the computational procedure described in Section 2.2 is followed (see Fig. 1). Since the

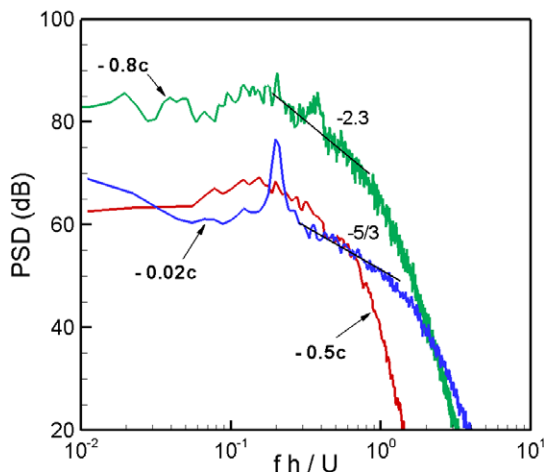


Fig. 8. Power spectral density spectra of wall pressure fluctuations at $x/c = -0.8$, -0.5 , and -0.02 .

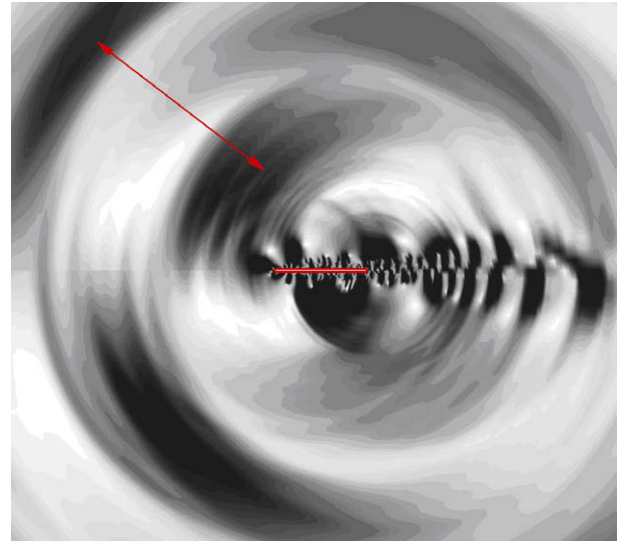


Fig. 9. Instantaneous pressure fluctuation field around the plate (located at the figure center); $\Delta p' = (P + p') - \overline{(P + p')}$.

microphone is located at $20c$ from the plate, the 2D acoustic field computed by the LPCE for the domain of $10c$ needs to be extrapolated to $20c$ and also to be corrected for 3D spectral pressure. Finally, the 3D spectral pressure radiated by the simulated span h needs to be corrected for the total span $100h$ (or $3c$) employed in the experiment. This procedure requires information on the spanwise coherence function of the surface pressure, $\gamma(z)$ in the most dominant noise source region, i.e. the trailing-edge of the plate. In Fig. 10, $\gamma(z)$ is compared between the computation for span h and the experiment for span $100h$ (or $3c$). This comparison confirms that at most frequencies, the spanwise coherence functions drop rapidly, except at the tonal frequency around $St = 0.2$. The spanwise coherence length of the surface pressure, $L_c(\omega)$ is then calculated by a Gaussian law, $\gamma(z) = \exp\{-z/L_c(\omega)\}^2$. The largest value of $L_c(\omega)$ is approximately estimated as $7h$ at $St = 0.2$ but in most cases, $L_c(\omega)$ is below h . This indicates that there exist a computational difficulty when a physical spanwise coherence length far exceeds the simulated span. Finally, the $SPL_c(\omega)$ is then calculated by Eq. (16) with $L_c(\omega)$, instead of $L'_c(\omega)$. In Ref. [21], the difference between $L_c(\omega)$ and $L'_c(\omega)$ is quantified and its sensitivity to the far-field SPL is discussed for 3D cylinder cross-flow noise at $Re_D = 46,000$ and $M = 0.21$.

The far-field SPL spectrum for the actual span $3c$ is now compared in Fig. 11 with the measured data of the Ecole Centrale de Lyon [7]. The numerical results are signal-processed by applying a hanning window function with the sampling frequency of 50 kHz, the block length of 0.04 s, and the number of averages of 10. The agreement is found excellent, especially for the match of the tonal peak (peak level deviation is 2.7 dB), its spectral broadening, as well as the other broadband part. This comparison indicates that not only the noise sources but also their turbulence statistics are well captured by the incompressible LES, while the propagation, scattering, and diffraction of the acoustic waves around the plate are accurately computed by the LPCE with other far-field SPL prediction procedures described in Section 2.2. It is also interesting to note that the tone at $St = 0.2$ outstands the broadband noise by 30 dB, despite of the fact that the wall pressure PSD at the trailing-edge is about 10 dB lower than that at the reattachment point (see Fig. 8). This is due to the differences in the spanwise coherence length presented by Fig. 10 and the distance of the reattachment point from the trailing-edge, i.e. negligible edge-scattering effects.

The directivity patterns at $r = 20c$ are also presented in Fig. 12 for various Strouhal numbers (or ratios of the plate chord length to

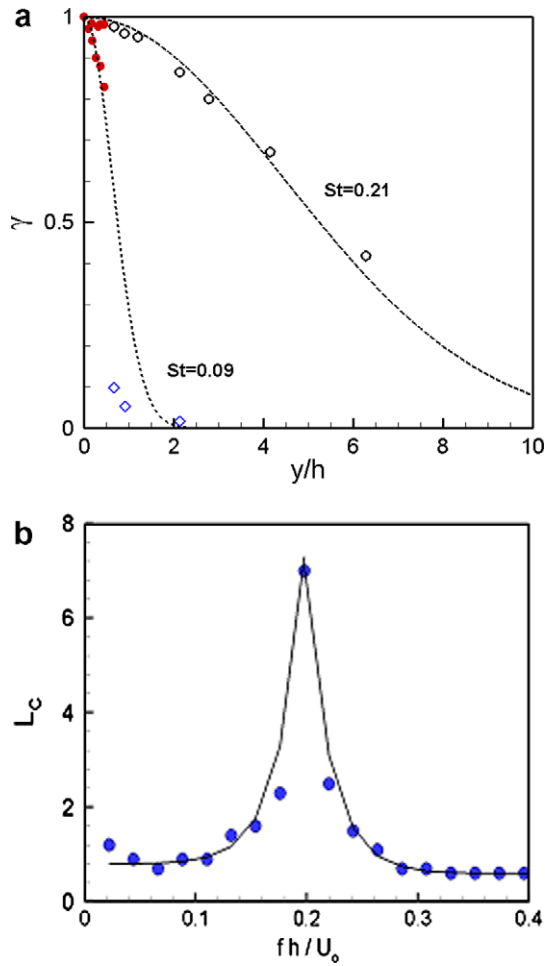


Fig. 10. Spanwise coherence functions (solid: compt., hollow: Exp., line: fitted) (top); spectral distribution of spanwise coherence length (symbol: compt., line: fitted) (bottom); both evaluated with the wall pressure at the trailing-edge.

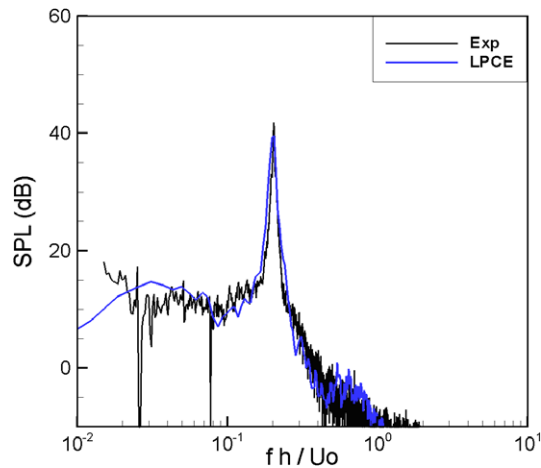


Fig. 11. Sound pressure level spectrum at $r = 20c$ vertically away from the mid-chord of the plate; computation (blue), experiment (black). (For interpretation of the references to colour in this figure legend, the reader is referred to the web version of this article.)

the acoustic wavelength). At vortex shedding frequency ($St = 0.2$ or $c/\lambda = 0.4$), it represents a clear dipole. As the Strouhal number increases or the acoustic wavelength becomes shorter than the chord length, the waves diffracted at the leading and trailing-edge of the plate are well captured; the directivity pattern changes to a

finger-like shape. It is worth noting that the first two plots of $St = 0.2$ and 0.4 are consistent with what is expected from analytical modeling based on zero-thickness assumption, as shown for instance in the study of Roger and Moreau [26]. At higher Strouhal numbers, the directivity pattern departs from the analytical results, essentially by showing a secondary beaming around 45° and 30° at $St = 1$ and 2 , respectively. This could be attributed to the plate thickness.

4.2. Forward-facing step noise

The flow and acoustics of the forward-facing step (experiment described in Section 3.2) are computed for Reynolds number based on the step height ($h = 0.012$ m), $Re_h = 8000$ and free stream Mach number, $M = 0.03$ ($U_0 = 10$ m/s). The incompressible large eddy simulation domain extends from $-100h$ to $100h$ in the streamwise direction, from 0 to $100h$ in the normal direction, and from 0 to $4h$ in the spanwise direction, respectively. The forward-facing step stands at $(x, y) = (0, 0)$. At the inlet, a uniform flow condition is imposed, and along the wall boundary, a non-slip boundary condition is applied from $x = -44h$ to match the experiment: a laminar boundary layer thickness, $\delta = 0.63h$ at $x = -10h$. A flow periodicity is assumed at the spanwise boundaries and a constant pressure condition is applied at the top and exit boundaries. In the present computation, 3.8 million mesh points are non-uniformly distributed with minimum normal grid spacing of $0.002h$ to keep $\Delta y_{min}^+ \sim 1$. The grid points are clustered from the step-edge to $7h$ downstream to resolve the shear layer instability and transition to turbulences. The computational domain is decomposed into 62 blocks for parallel computation and each block is assigned with $31 \times 41 \times 51$ points in x -, y -, and z -directions. The LES computation is conducted with $\Delta t = 6 \times 10^{-7}$ s for 600,000 iterations (or 0.36 s).

The three-dimensional, instantaneous flow structures over the step are presented in Fig. 13 (top) by the iso-surfaces of Q , the second invariant of the velocity gradients. By Kelvin–Helmholtz instability, a shear layer emanated from the step-edge becomes unstable in the streamwise direction and starts to break-off into small-scale eddies at $x/h = 1$. One can notice that the separated shear layer re-attaches around $x/h = 2.5$ and the boundary layer becomes turbulent as it approaches downstream; the hair-pin vortices are clearly discernable in the boundary layer. Fig. 13 (bottom) shows three-dimensional surface streamlines in the frontal region of the step; as pointed out by Stüer et al. [11] and Chou and Chao [27], the stagnation line over the front surface branches off in the spanwise direction and the front vortex breaks out of the separation bubble in longitudinal streaks, triggering the spanwise instability of the separated shear layer over the step.

In order to quantify the pressure fluctuations over the forward-facing step, the wall pressure fluctuations are monitored at position 1 ($x/h = -1$) in front of the step and 3, 4, and 5 ($x/h = 1.5, 2.5,$ and 4) over the step. The power spectral density (PSD) spectra (spanwise-averaged) are presented in Fig. 14. One can notice that the pressure fluctuations in the re-circulating zone are much weaker than those over the step surface, implying that the bifurcating nature of the re-circulating zone mentioned by Stüer et al. [11] is not significantly related to the dynamics of the flow. Also, the wall pressure PSD spectrum recorded at position 1 exhibits no significant energy level, except a very small peak at $St(= fh/U_0) = 0.1$ due to the pressure fluctuations induced by the shear layer flapping over the step.

The dominance of the pressure fluctuations occurs at position 4, where small-scale eddies from the shear layer merge into the large-scale vortices via vortex coalescences near the reattachment point. One can notice in Fig. 14 that the PSD level at position 4 is increased by 5–10 dB at $St < 0.6$ – 0.7 , in comparison with those at position 3 and 5. After the reattachment point (position 5), the

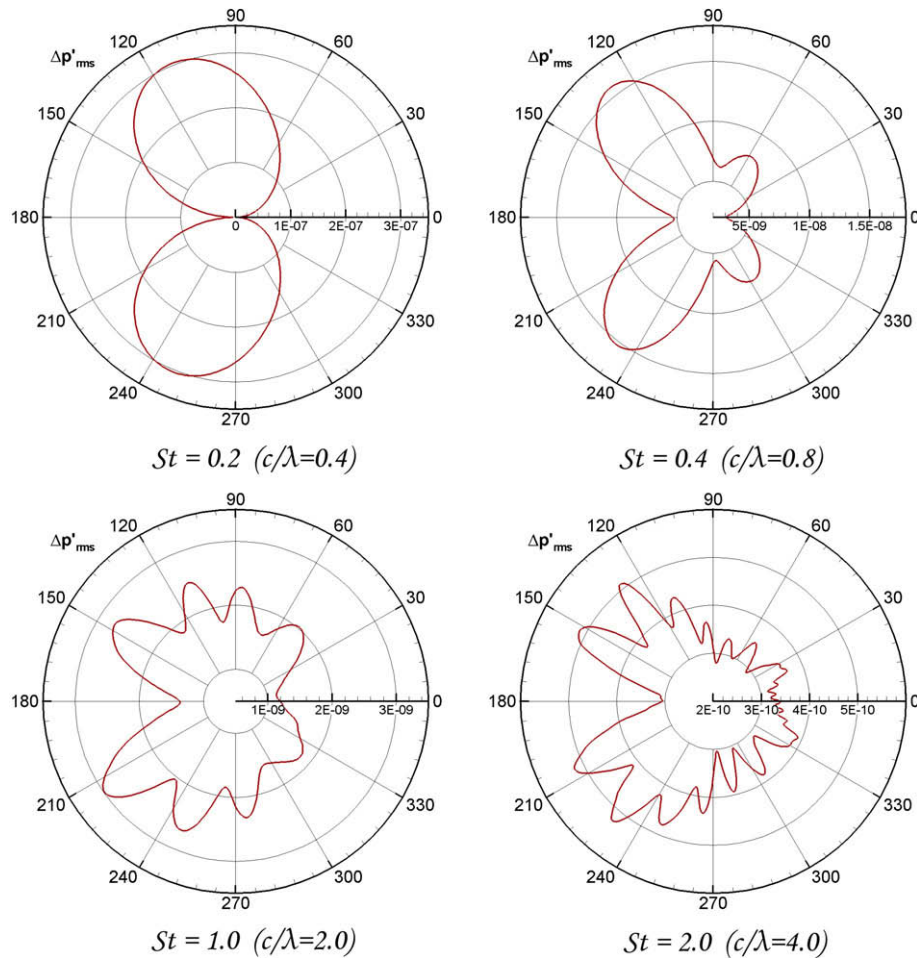


Fig. 12. Directivity patterns of $\Delta p'_{rms}$ at $r = 20c$ for different Strouhal numbers.

PSD level drops back at $St < 0.6$ – 0.7 , whereas at higher frequencies (i.e. 0.6 – $0.7 < St < 2$), the decaying rate changes from -8 to -5 and finally up to -2.3 , indicating that the coalescent eddies at the reattachment point are now breaking into smaller ones in the downstream boundary layer. It seems that through the dynamical changes, the leading-edge separation bubble shows strong three-dimensional, transient vortex-wall interactions near the reattachment point.

An acoustic field is now solved by the linearized perturbed compressible equations (LPCE). The computation is carried out with the same time $\Delta t = 6 \times 10^{-7}$ s for the last 400,000 iterations (or 0.24 s) of LES data. The acoustic grid is consisted of 541×181 points, distributed in the domain from $-200h$ to $200h$ (streamwise) and from 0 to $200h$ (normal), with minimal normal grid spacing at the wall 10 times larger than that of the hydrodynamic grid. This grid-splitting technique largely relieves the time step constraint and is therefore computationally very efficient for low Mach number aeroacoustic problems.

Fig. 15 shows an instantaneous field of pressure fluctuations ($\Delta p' = p - \bar{p}$) over the forward-facing step. There is no clear tone or directivity presented in the wave radiation, indicating a broadband nature of the forward-facing step noise. As confirmed by Fig. 16, the SPL spectrum at $r = 83h$ vertically away from the step-edge is quite broadband. The blue curve¹ (solid) corresponds to the LPCE solution at zero wave-number space, while the red curve

(dashed) represents the SPL spectrum corrected by Oberai et al. formula [19] for 3D wave propagation. It is interesting to note that the 2D spectrum closely resembles the -2.3 decaying rate of the wall pressure PSD spectrum at $x/h = 5$ between 0.6 – $0.7 < St < 2$, and after the 3D wave correction, the slope changes from -2.3 to -1.8 because the 3D correction formula, Eq. (11) has a frequency dependency, i.e. $\sim \sqrt{\omega}$. Hence, the PSD level decreases at low frequency and this results in a broad peak around $St = 0.6$ – 0.7 in the final SPL spectrum. It is interesting to note that this frequency actually coincides with the most unstable mode of the shear layer instability [28], i.e. $\omega\delta/c = 0.42$, which equals to $St = 0.64$, based on the shear layer thickness ($\delta = 0.06h$) and the convection velocity ($c_e = 0.67U_o$) obtained by the present computation. Here, ω is the angular frequency, and the convection velocity c_e was determined by taking an average of the slopes of the wall pressure fluctuations over the step plotted in x – t space (see Fig. 17). The slope was estimated for the region (i.e. $1 < x/h < 2$), which shows the footprints of the pressure fluctuations of the shear layer breaking-off.

By examining the spectral characteristics of the wall pressure fluctuations and the far-field SPL spectrum, it is observed that the leading-edge separation bubble is composed of various unsteady flow characteristics; (i) shear layer is flapping at $St = 0.1$, (ii) shear layer is breaking-off into small-scale eddies at $St = 0.6$ – 0.7 ($x/h = 0.1$), (iii) small-scale eddies are merging into large-scale eddies via vortex coalescences at $0.2 < St < 0.5$ (near the reattachment point, $x/h = 2.5$), (iv) coalescent vortices are breaking into smaller-scale eddies in the downstream boundary layer with a decaying rate of -2.3 at 0.6 – $0.7 < St < 2$. Among these, the

¹ For interpretation of color in Fig. 16, the reader is referred to the web version of this article.

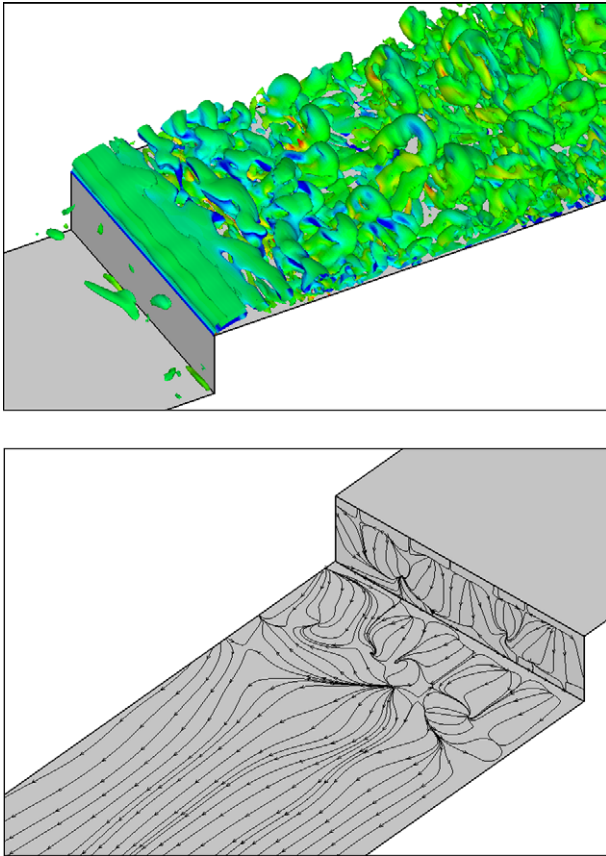


Fig. 13. Instantaneous Q iso-surfaces over the forward-facing step (top); surface streamlines in front of the forward-facing step (bottom).

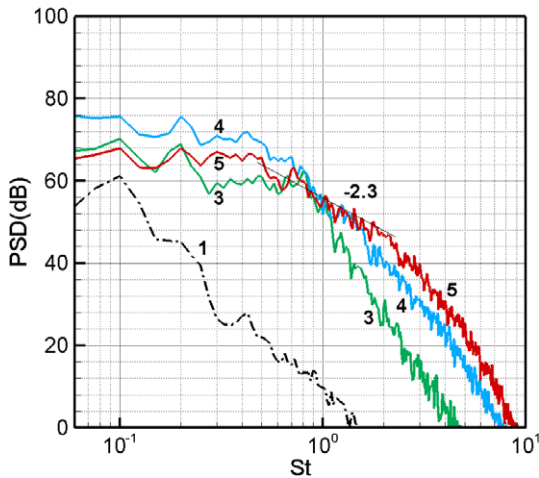


Fig. 14. Power spectral density spectra of wall pressure fluctuations (spanwise-averaged); positions 1, 3, 4, and 5.

unsteady flow characteristic associated with (ii) seems to be the original source of the forward-facing step noise because (i), (iii), and (iv) occur as a hierarchical consequence.

The present prediction is now confirmed with the experimental SPL spectrum measured at the University Erlangen [8]. In order to predict the SPL spectrum for the total span ($L = 20.8h$) employed in the experiment, the spanwise coherences of the wall pressure fluctuations at three representative frequencies, $St = 0.1, 0.45, \text{ and } 0.8$ are plotted in Fig. 18 (from the top) for the entire surface of the for-

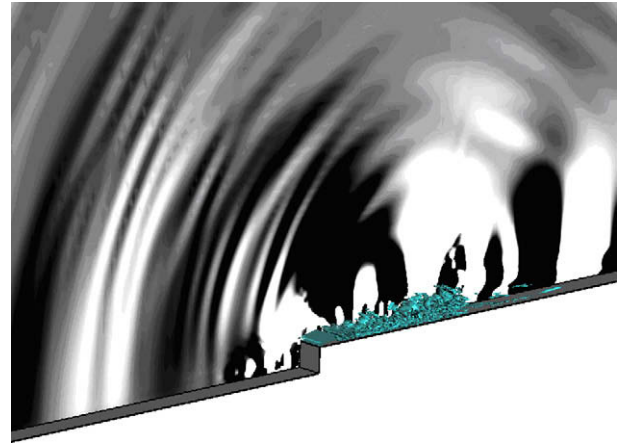


Fig. 15. Instantaneous pressure fluctuation field around the forward-facing step, $\Delta p'$.

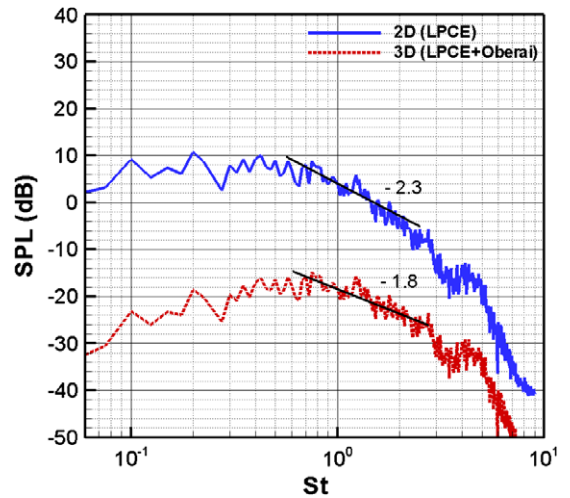


Fig. 16. Sound pressure level spectra at $r = 83h$ vertically away from the step-edge; 2D (solid), 3D corrected (dashed).

ward-facing step. As shown in the figure, γ at $x/h = 2.5$, which is selected as a representative case, indicates that the spanwise coherence lengths (L'_c/L_s) at all frequencies do not exceed $1/\sqrt{\pi} \approx 0.5642$ in Eq. (17), although there is a dependence of the coherence length on St . So, the final SPL spectrum is corrected by simply adding $10 \log N = 10 \log(20.8/4) \approx 7.16$ dB to the red curve (dashed) in Fig. 16.

Fig. 19 shows that the forward-facing step noise measured over the background noise (red, slope: -2) is appearing as a hump (blue) over the frequency range between 0.6 and 6 in Strouhal number with a slope close to -1.7 to -1.8 . As presented in Fig. 16, the decaying slope of the computed SPL spectrum at $0.6-0.7 < St < 2$ changes from -2.3 to -1.8 after 3D wave correction and as a consequence, the spectrum (green) predicted by the present method agrees reasonably with the experimental data in the hump region. The present comparison shows a lack of spatio-temporal resolutions higher than $St = 3$ but it supports well the prediction capabilities of the proposed LES/LPCE hybrid method.

5. Conclusion

The present study has demonstrated that a low-subsonic, turbulent flow noise can be accurately as well as efficiently predicted

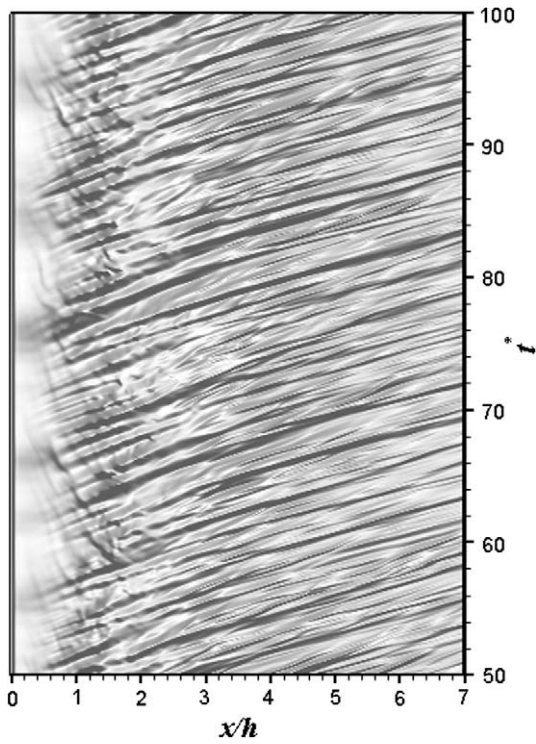


Fig. 17. Wall pressure fluctuations over the forward-facing step in $x-t$ space, $t^* = tU_o/h$.

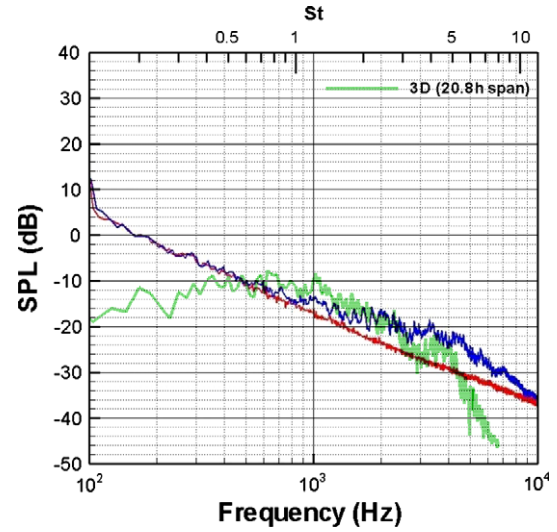


Fig. 19. Sound pressure level spectra at the measurement point; present (green, dotted), Exp. (blue), background noise (red). (For interpretation of the references to colour in this figure legend, the reader is referred to the web version of this article.)

by the present LES/LPCE hybrid method. In this method, the acoustic sources are represented by a material derivative of the turbulent, hydrodynamic pressure fluctuations (i.e. DP/Dt) computed by the incompressible large eddy simulation (LES). No numerical instability were observed in LPCE computations because any

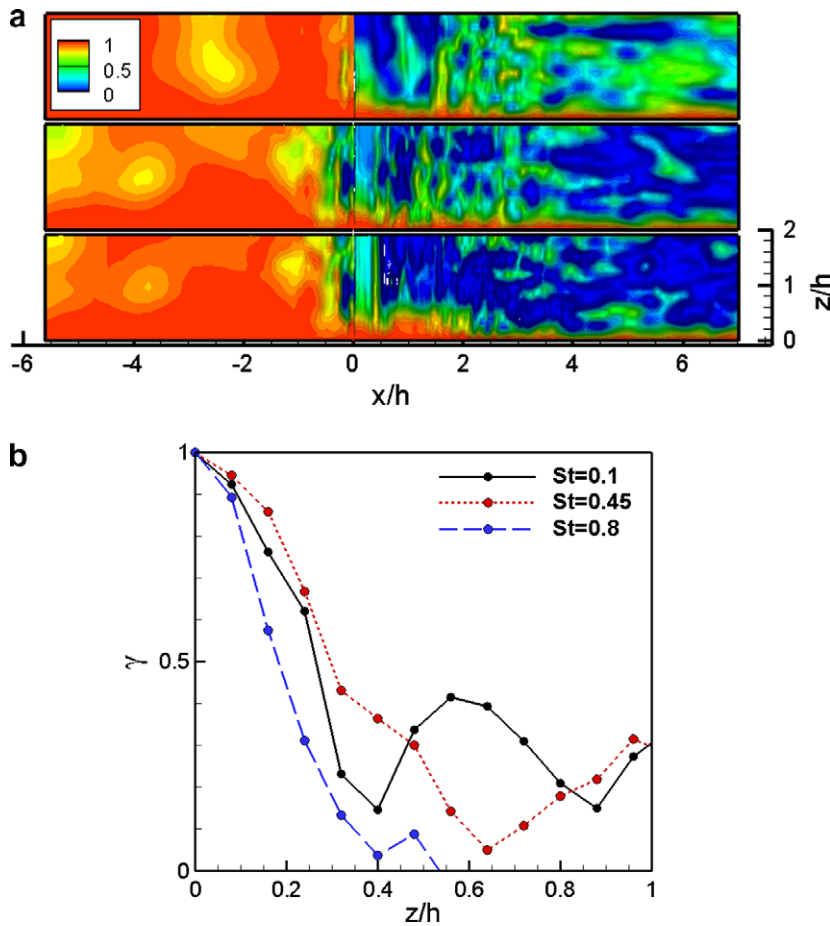


Fig. 18. Spanwise coherence field of wall pressure fluctuations at $St = 0.1, 0.45,$ and 0.8 (from the top); spanwise coherence function at $x/h = 2.5$ (bottom).

sources related to produce the perturbed vorticity are eliminated in the formulation. Moreover, not only the generation and propagation of the acoustic waves but also their scattering, diffraction, and refraction effects can be directly computed by the present method. The validity of the far-field noise prediction methods discussed in Section 2.2 are also confirmed by comparing the predicted far-field sound pressure level spectra with the experimental data. Two cases of experiments considered in this study are found very valuable in validating a CAA method for predicting the broadband airframe noise at low-subsonic, turbulent flow conditions.

Acknowledgement

This work was supported by the Korea Research Foundation Grant funded by the Korean Government (MOEHRD, Basic Research Promotion Fund) (KRF-2008-013-D00015).

References

- [1] Hardin JC, Pope DS. An acoustic/viscous splitting technique for computational aeroacoustics. *Theor Comput Fluid Dyn* 1994;6:323–40.
- [2] Shen WZ, Sorenson JN. Aeroacoustics modeling of low-speed flow. *Theor Comput Fluid Dyn* 1999;13:1057–64.
- [3] Slimon SA, Soteriou MC, Davis DW. Computational aeroacoustics simulations using the expansion about incompressible flow approach. *AIAA J* 2000;37:409–16.
- [4] Seo JH, Moon YJ. Perturbed compressible equations for aeroacoustic noise prediction at low mach numbers. *AIAA J* 2005;43:1716–24.
- [5] Seo JH, Moon YJ. Linearized perturbed compressible equations for low mach number aeroacoustics. *J Comput Phys* 2006;218:702–19.
- [6] Ewert R, Schröder W. Acoustic perturbation equations based on flow decomposition via source filtering. *J Compt Phys* 2003;188:365–98.
- [7] Roger M, Moreau S, Guédel A. Vortex-shedding noise and potential-interaction noise modeling by a reversed sears' problem. *AIAA-Paper* 2006-2607.
- [8] Becker S, Escobar M, Hahn C, Ali I, Kaltenbacher M, Basel B, et al. Experimental and numerical investigation of the flow induced noise from a forward facing step. *AIAA-Paper* 2005-3006.
- [9] Casalino D, Jacob M. Prediction of aerodynamic sound from circular rods via spanwise statistical modelling. *J Sound Vib* 2003;262:815–44.
- [10] Jacob MC, Boudet J, Casalino D, Michard M. A rod-airfoil experiments as a benchmark for broadband noise modeling. *Theor Comput Fluid Dyn* 2005;19:171–796.
- [11] Stüer H, Gyr A, Kinzelbach W. Laminar separation on a forward facing step. *Eur J Mech B/Fluids* 1999;18:675–92.
- [12] Lele SK. Compact finite difference schemes with spectral-like resolution. *J Comput Phys* 1992;103:16–42.
- [13] Gaitonde D, Shang JS, Young JL. Practical aspects of high-order numerical schemes for wave propagation phenomena. *Int J Numer Methods Eng* 1992;45:1849–69.
- [14] Edgar NB, Visbal MR. A general buffer zone-type non-reflecting boundary condition for computational aeroacoustics. *AIAA-Paper* 2003-3300.
- [15] Perot F, Auger JM, Giardi H, Gloerfelt X, Baily C. Numerical prediction of the noise radiated by a cylinder. *AIAA-Paper* 2003-3240.
- [16] Ewert R, Schröder W. On the simulation of trailing edge noise with a hybrid LES/APE method. *J Sound Vib* 2004;270:509–24.
- [17] Manoha E, Delahay C, Sagaut P, Mary I, Khelil S, Guillen P. Numerical prediction of unsteady flow and radiated noise from a 3d lifting airfoil. *AIAA-Paper* 2001-2133.
- [18] Seo JH, Moon YJ. Prediction of low mach number turbulent flow noise using the splitting method. *AIAA-Paper* 2004-2860.
- [19] Oberai AA, Rohnaldin F, Hughes TJR. Trailing-edge noise due to turbulent flows. Technical report, Report No. 02-002, Boston University; 2002.
- [20] Scott JN, Pilon AR, Lyrintzis AS, Rozmajzl TJ. A numerical investigation of noise from a rectangular jet. *AIAA-Paper* 1997-285.
- [21] Seo JH, Moon YJ. Aerodynamic noise prediction for long-span bodies. *J Sound Vib* 2007;306:564–79.
- [22] Kato C, Iida A, Takano Y, Fujita H, Ikegawa M. Numerical prediction of aerodynamic noise radiated from low mach number turbulent wake. *AIAA-Paper* 1993-145.
- [23] Visbal MR, Rizzetta DP. Large-eddy simulation on curvilinear grids using compact differencing and filtering schemes. *J Fluids Eng* 2002;124:836–47.
- [24] Na Y, Moin P. The structure of wall-pressure fluctuations in turbulent boundary layers with adverse pressure gradient and separation. *J Fluid Mech* 1998;377:347–73.
- [25] Farabee TM, Casarella MJ. Spectral features of wall pressure fluctuations beneath turbulent boundary layer. *Phys Fluids A* 1991;3:2410–20.
- [26] Roger M, Moreau S. Back-scattering correction and further extensions of Amiet's trailing-edge noise model. Part 1: theory. *J Sound Vib* 2005;286:477–506.
- [27] Chou JH, Chao SY. Branching of a horseshoe vortex around surface-mounted rectangular cylinders. *Exp Fluids* 2000;28:394–402.
- [28] Blake WK. *Mechanics of flow-induced sound and vibration*, vol. 1. Orlando: Academic Press; 1986.